Accurate and unequivocal determination of the crystal-field parameters of lanthanide ions via a multitechnique approach

Michael Slota,[1,2,*] Shang-Da Jiang,[2] Eric Heintze,[2] Yvonne Rechkemmer,[3] Martin Dressel,[2] Joris van Slageren,[3] and Lapo Bogani[1]

[1]*Department of Materials, University of Oxford, 16 Parks Road, Oxford OX1 3PH, United Kingdom*
[2]*1.Physikalisches Institut, Universität Stuttgart, Pfaffenwaldring 57, 70569 Stuttgart, Germany*
[3]*Institut für Physikalische Chemie, Universität Stuttgart, Pfaffenwaldring 55, 70569 Stuttgart, Germany*

(Received 18 September 2018; revised manuscript received 6 February 2019; published 5 April 2019)

Understanding the crystal field of lanthanide complexes is pivotal for the testing of Stevens operator equivalents and the development of lanthanide-based molecular magnets. Intense theoretical investigation is aimed at the determination of the Hamiltonian parameters, but accurate experimental tests often suffer from overparametrization. Because of this, clear-cut experimental determinations are missing even high-symmetry environments. Here we present a detailed study of the crystal-field parameters of Pr(III) ions in a high-symmetry environment, using the cyano-based molecular magnetic material $Pr[Co(CN)_6] \cdot 5H_2O$. The problem of multiple solutions is considered with particular detail, and we show how unequivocal determination of the parameters becomes possible only by combining different spectroscopic and magnetometric techniques. Eventually we compare the solution with fitting methodologies that are commonly employed and we highlight the level of information that can be gained by such procedures.

DOI: 10.1103/PhysRevB.99.134410

I. INTRODUCTION

Rare-earths (REs) are exceptionally suited to creating magnetic materials [1], because they offer high anisotropies [2] and high-spin ground states [3], and, as a consequence, they find application in several commercial magnetic alloys [4]. When they are included into coordination complexes, their magnetic properties can be tuned with the tools of molecular chemistry: since the discovery of the first lanthanide-based complexes with slow relaxation of the magnetization [5], the use of REs in the synthesis of single-molecule magnets has boomed [1–3,6–10], and they have been employed in molecular spintronic [11–13] devices, photoswitchable magnetic chains [14], nuclear spin manipulation schemes [15,16], and the creation of molecular magnets with record values of the blocking temperature [17–19]. These molecular nanomagnets can be functionalized with different chemical groups, so as to tailor their chemophysical properties [20] in order to attach them onto surfaces [21,22], sandwitch them between electrodes [12,13] and control them via external stimuli, such as magnetic or electric fields, temperature, pressure or light [23–28]. Finally, quantum coherence properties can be tuned promoting phase-memory times in the microsecond regime [29–34], a crucial requirement for potential quantum applications.

Understanding the interactions between the lanthanide ions and their crystal-field environment is crucial not only to optimize the magnetic response, but also to rationalize their behavior on surfaces or inside spintronic devices. The magnetic properties of REs are determined by the electronic orbitals occupied by the $4f$ electrons. The energy splitting of the resulting states is mainly affected by Coulomb interactions, spin-orbit coupling and the electrostatic potential generated by the surrounding crystal-field as indicated in Fig. 1(b). Due to the localized nature of $4f$ electrons, electron repulsion interactions ($\sim 10\,000\,cm^{-1}$) and spin-orbit coupling ($\sim 1000\,cm^{-1}$) dominate over crystal-field interactions ($\sim 100\,cm^{-1}$) [35]. As a result, the spin eigenfunctions $|\Psi_S\rangle$ do not correspond to the simple $|M_J\rangle$ levels, but need to be expressed as a weighted combination of all $|M_J\rangle$s. Determining these combinations is highly nontrivial, and makes the precise modeling of the magnetic properties particularly difficult. Furthermore, due to spin-orbit coupling, a strong crystal-field may cause a substantial coupling of different Coulomb terms. Only in favourable cases, where either the spin-orbit coupling induced J mixing is negligible, or the crystal-field splitting is small and the intermediate coupling model can be employed, the Russell-Saunders coupling scheme can be utilised and Stevens operator equivalents formalism can be used to describe the level splitting of a rare-earth system [36]. However, more accurate results are obtained when J mixing is considered. Therefore we will take advantage of the Racah tensor formalism in this studies [35]. Efforts are underway to establish a general theoretical model for all lanthanide ions, which can explain the magnetic properties from the analysis of the crystal field, and a few theoretical frameworks have been developed. Effective electrostatic models of point charges around a rare earth ion [37] and novel computational packages that perform calculations for first-order unquenched orbital moments, and use electronic terms as the basis states for each ion [38], as well as more traditionally known *ab initio* techniques [39], are displaying their power, and opening new perspectives in the field [40–44].

*michael.slota@materials.ox.ac.uk

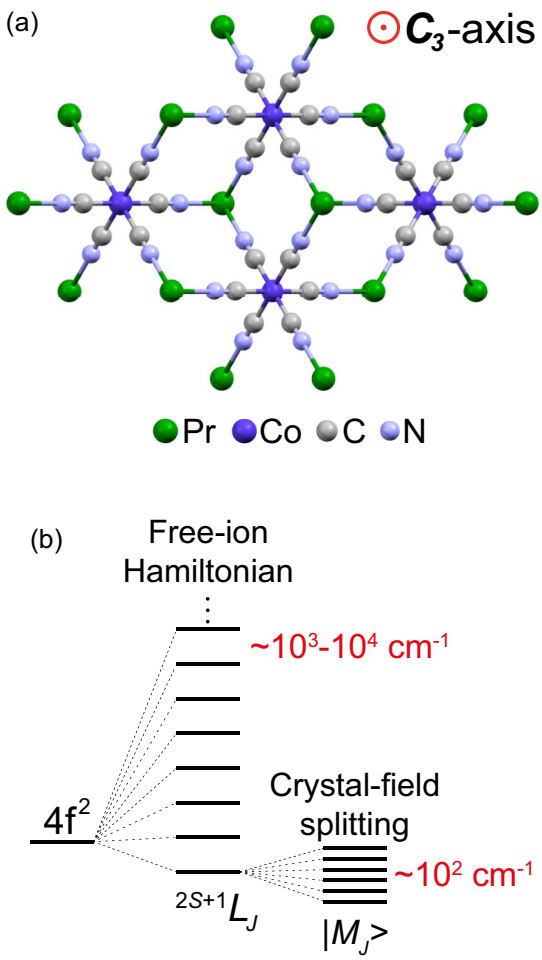

FIG. 1. (a) Crystal structure of (*ab* plane) of $Pr[Co(CN)_6] \cdot 5H_2O$, as obtained via x-ray crystallography and viewed along the crystallographic C_3 symmetry axis. Water molecules are omitted for clarity. (b) Scheme of the origin of the splitting of the energy levels of the Pr(III) ions. Electron-electron interactions produce Russell-Saunders states for the free-ion Hamiltonian. Additionally, states with the same J coming from different Coulomb terms are mixed by spin-orbit coupling, and the crystal field splits the J multiplets, as described by Eqs. (3) and (4) in the text.

Validation of these models is also quite challenging, because it requires a very precise experimental determination of all the crystal-field parameters of the spin Hamiltonian. When using the standard formalism of Stevens operators, there is no guarantee that the resulting series of spherical harmonics will converge, or that higher-order, low-symmetry terms will be less important than lower-order ones. As a result, extraction of the crystal-field parameters is basically impossible with just magnetometric techniques, and the very large linewidths of REs prevent the use of standard electron paramagnetic resonance (EPR) spectroscopy. The problem becomes even more challenging when one considers that, in order to validate models, it is necessary not only to have the full series of operators, but to check the sign of coefficients.

Spectroscopy allows direct observation of the magnetic level splittings [45–49], but the determination of the magnetic state mixing via spectroscopic means remains very challenging. This level of information is presently obtainable only by using large scale facilities, e.g., via neutron scattering techniques [23,50]. Here we show how a detailed analysis of the crystal-field interaction parameters is made possible via a comprehensive experimental investigation that combines multiple spectroscopic techniques and magnetic measurements. We present an iterative approach that takes advantage of magnetometry analysis combined with spectroscopic techniques such as terahertz (THz) absorption, magnetic circular dichroism (MCD) and low-temperature electronic absorption. To this purpose, we use the model compound $Pr[Co(CN)_6] \cdot 5H_2O$, where the number of terms in the crystal-field Hamiltonian is reduced because of the crystallographic space group with high, hexagonal symmetry (D_{3h}). The methodology is anyway exportable to other molecules, where the lanthanide ion is in a low symmetry environment [8]. A full description of the crystal field in such lower symmetry complexes would require the investigation of more transitions, and the inclusion of up to 27 crystal-field parameters in the iterative method. In this work, we concentrate on the four crystal-field parameters necessary for the D_{3h} symmetry, which is fundamental for the magnetic behavior of many frustrated lattices.

II. EXPERIMENTS

The family of $Ln[Co(CN)_6] \cdot 5H_2O$ complexes offers regular hexagonal symmetry, and is thus quite suited to our purposes. Moreover, the Co(III) ions are in a diamagnetic low-spin configuration, so that the only magnetic contribution arises from the trivalent lanthanide centers. In this study, we will focus on the praseodymium derivative, whose structure is shown in Fig. 1(a).

Crystals were obtained [51,52] from a 0.1 M aqueous solution of $K_3[Co(CN)_6]$ and $Pr[NO_3]_3 \cdot 6H_2O$, whose pH was adjusted to 5 using nitric acid, in order to control the crystallization rate. Under ambient conditions, $Pr[Co(CN)_6] \cdot 5H_2O$ slowly dehydrates into $Pr[Co(CN)_6] \cdot 4H_2O$, and the transformation lowers the hexagonal site symmetry (D_{3h}) to an orthorhombic one [51]. The process can be easily monitored optically, as the crystal appearance changes over the course of days. In order to prevent this from happening, crystals were kept in their mother solution until the experiments. No degradation was observed at temperatures (T) below 273 K. See Supplemental Material for crystallographic data [53].

A. Magnetometry

A first qualitative insight into the nature of the ground state can be obtained from the magnetic anisotropy of the system at low T. A low $|M_J\rangle$ ground state results in an anisotropy of xy-type, while a large value yields an Ising-type anisotropy. The T dependence of the magnetization of a pressed pellet sample, measured using a Quantum Design MPMS-XL7 SQUID magnetometer in a magnetic field of 5000 Oe is shown in Fig. 2(a). At 5000 Oe, the magnetic response of the sample is linear and far away from saturation (see Supplemental Material [54]). The magnetic susceptibility χ can thus be considered as $\chi = M/H$, where M represents the magnetic moment.

More information can be extracted from the angular dependence of the susceptibility. To this purpose, a single crystal

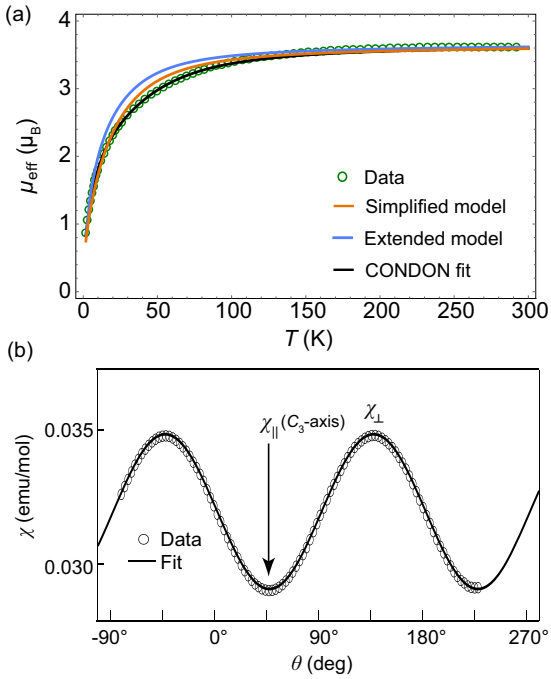

FIG. 2. Magnetic response of the system. (a) Temperature dependence of the effective magnetic moment μ_{eff} per ion, displayed as in multiples of the Bohr magneton μ_B, as measured on a pressed pellet. The agreement with different theoretical calculations is provided: the simplified model (red) considers the first 33 states ($^3H_4$, $^3H_5$, and $^3H_6$); the extended model(blue) uses the B_q^k parameters determined from spectroscopic techniques and considers the first 91 states; the black line represents a least-square fit by CONDON. (b) Angle-resolved SQUID measurement of a single crystal sample (mass $m = 6.89$ mg, $T = 3$ K). Due to its uniaxial anisotropy, the principal susceptibilites can be obtained as denoted in the figure. $\chi_{||}$ and $\chi_\perp$ correspond to the susceptibility parallel and perpendicular to the C_3 axis, respectively.

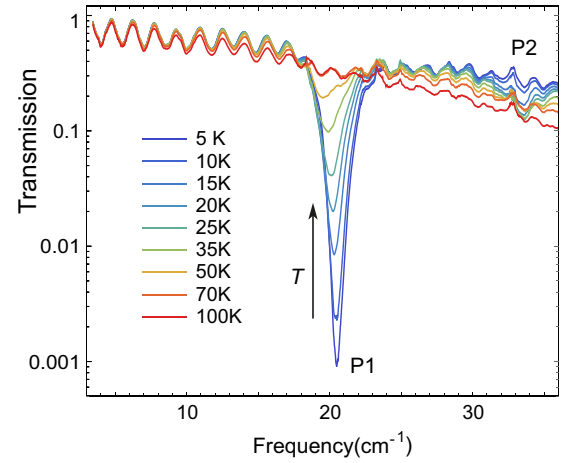

FIG. 3. Transmission spectrum of a pressed pellet sample (with 5 mm diamater and 1.53 mm thickness) in zero field, recorded between 3 and 36 GHz at temperatures between 5 and 100 K, showing the presence of two peaks: the strong absorption around 20.5 GHz (labeled as P1) and a much weaker absorption region around 33.5 GHz (labelled P2).

was fixed on an L-shaped CuBe support on the Quantum Design MPMS Horizontal Rotator using Apiezon N grease. The measurement was carried out at $T = 3$ K and $H = 5000$ Oe, so that the magnetic behavior is solely related to the ground state. Due to the hexagonal symmetry of the crystal, the magnetic anisotropy is uniaxial with the crystallographic C_3 axis being a magnetic principal axis with susceptibility $\chi_{||}$. To directly obtain the principal susceptibilities $\chi_{||}$ and $\chi_\perp$, we rotated the crystal along an axis perpendicular to the C_3 axis. The magnetic susceptibility $\chi(\theta)$ then depends on the angle θ between a plane containing the C_3 axis and H. This technique allows us to determine the full susceptibility tensor with a single rotational measurement. The results of a full rotation is shown in Fig. 2(b), with data corrected for the diamagnetic background, mechanical slackness and zero position. In agreement with the planned crystal alignment, the C_3 axis is parallel to the magnetic field at $\theta = 47.7°$. By fitting of the data using the expression

$$\chi(\theta) = \chi_{||}\cos^2\theta + \chi_\perp \sin^2\theta - 2\chi_{xz}\cos\theta\sin\theta, \quad (1)$$

followed by a diagonalization procedure, we obtain $\chi_{||} = 2.90\times10^{-2}$ emu/mol and $\chi_\perp = 3.49\times10^{-2}$ emu/mol at 3 K. Despite the small magnetic anisotropy, we can still identify $\chi_{||}$ as the hard axis and $\chi_\perp$ as the easy axis. The observed anisotropy excludes a ground state of $M_J = 0, \pm1$, which favours a strong easy-plane anisotropy. For heavier lanthanide ions, such as Dy(III) or Tb(III), the ground state would be identified more easily, because of their usually large spin state. However, for more isotropic systems such as Pr(III), further data obtained via more sensitive spectroscopic techniques are required, rather than using magnetic models to fit the energy levels solely to the magnetic data.

B. THz and far-IR spectroscopies

The typical energy level splittings of $4f$ multiplets lie in the 100-cm^{-1} regime, and THz spectroscopy (0.03–1.5 THz, 1–45 cm^{-1}) enables in-depth investigation of the magnetic states. This technique has been previously used on various magnetic systems to obtain the energy level splitting [55–57], but has been unable, to date, to provide a complete set of anisotropy coefficients, and thus the spin wave functions.

Measurements on pressed pellet samples are shown in Fig. 3. A set of different backward-wave oscillators (BWOs) served as THz sources, each covering a certain wavelength regime. For measurements in a magnetic field we used an Oxford Instruments Spectromag Split-Coil magnet SM4000 (fields up to 7 T), equipped with Mylar windows. For zero-field measurements, we used a home-built cryostat with tilted windows which suppress standing-wave effects in the spectrum. The THz radiation was detected using either a Golay cell or a helium-cooled bolometer. The transmission was recorded after taking a reference spectrum through a hole of same size [58]. Data are represented after applying a Savitzky-Golay filter in order to suppress noise arising from low output powers at certain wavelengths. Baseline oscillations arise from Fabry-Pérot resonances within the pellet sample, and can be fitted using Fresnel formulas [59]. An overall nonresonant electronic absorption of microwaves is also present, which increases both with T and frequency.

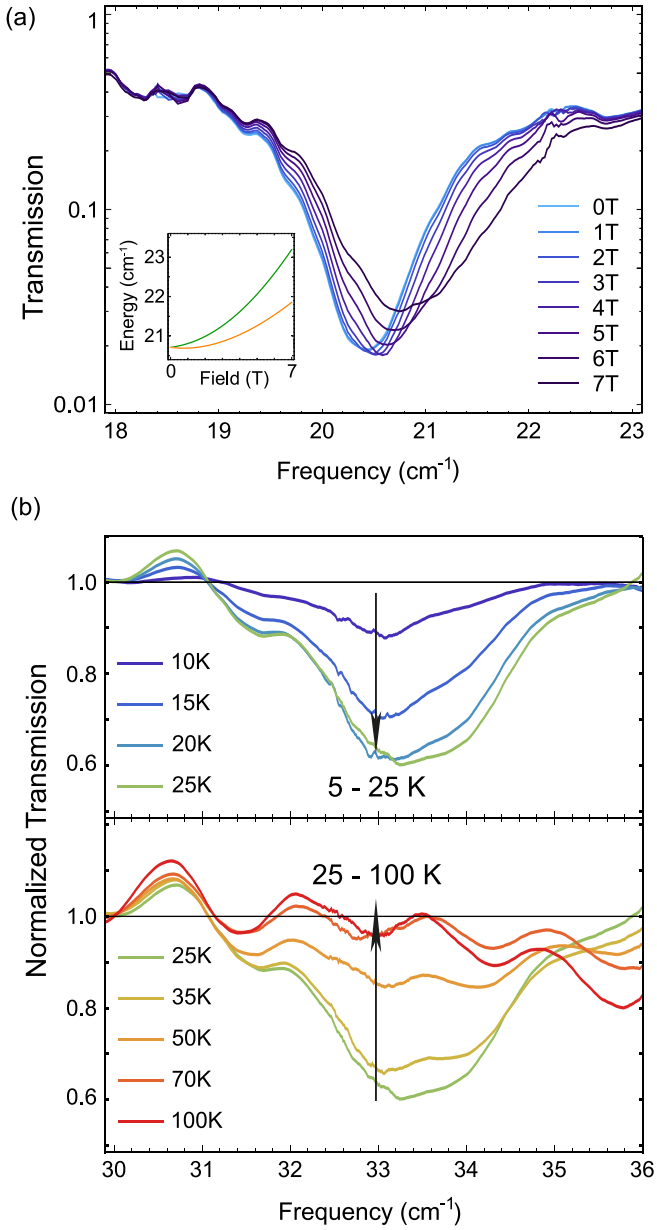

FIG. 4. (a) Zoom-in of the magnetic field dependence of peak P1, measured at 2 K between 0 and 7 T, showing the field dependence of the peak center. The inset shows the calculated transition energies from a doublet ground state as a function of the magnetic field, using the best set of crystal-field parameters. The green and orange curves correspond to the two lowest-lying states in a magnetic field. (b) Nonmonotonic behavior of the transmission spectrum of peak P2. All spectra are normalized relative to the 5 K measurement in zero field, in order to better show the variation.

The zero-field spectrum is shown in Fig. 3. Two prominent absorptive features appear at 20.5 and 33.1 cm^{-1} at 5 K, denoted as P1 and P2, respectively.

The magnetic field dependence of P1 [Fig. 4(a)] shows that the transition energy shifts towards higher frequencies at higher fields. As phonon absorptions are not affected by magnetic fields, this clearly identifies P1 as the first excited magnetic state, and magnetic dipole selection rules, $\Delta M_J = 0, \pm 1$, must apply. The broadening of the spectrum at higher magnetic fields can be explained with a doublet ground state, where both states are significantly populated even at large magnetic fields at 2 K. This observation is supported by a calculation of the transition energies using the crystal-field parameters discussed later. Furthermore, unresolved interactions, such as hyperfine anisotropy, or g-tensor anisotropy, could play a role here. It is interesting to notice the presence of a slight temperature-dependent change in energy of P1 (Fig. 3), which can be connected to a small lattice constant change at lower T, which slightly changes the crystal-field potential felt by the 4f electrons in this region.

The absorption at P2 shows a nonmonotonous dependence on T: when raising T from 5 K, the absorption increases until about 25 K [Fig. 4(b)], while, above 25 K, the absorption gradually diminishes again. This behavior is typical when in presence of a transition from a higher, thermally populated state, and we identify the peak as arising from the transition from the first excited to the second excited state. Considering a Boltzmann population of states, the first excited state becomes populated at $T > 7$ K, thus the absorption strength increases. As the electronic states get more equally populated when increasing T further, this transition vanishes above 100 K. We thus expect a second excited state, and another peak P2, at 53.7 cm^{-1} from the ground state.

Far-infrared transmission spectra were acquired on a Bruker IFS 113v Fourier Transform spectrometer equipped with an Oxford Spectromag 4000 Split-Coil magnet and Mylar windows, and unpolarized light in the frequency range 10–110 cm^{-1} was detected with a helium-cooled Bolometer with 0.5-cm^{-1} resolution, as described elsewhere [57]. The results at 5 K and at different magnetic fields, up to 7 T are shown in Fig. 5 (see also Supplemental Material [60]). As phonon excitations do not shift upon applying a magnetic field, transitions within the magnetic multiplet can be identified. The peaks already identified, with better resolution using THz spectroscopy, are visible and the far-infrared data confirm the observations. Figures 5(b) and 5(c) show the presence of a magnetic field evolution for peaks inaccessible with the BWOs and THz spectrometers. We can clearly identify the predicted peak P2, in the 53–56 cm^{-1} window [Fig. 5(b)]. This matches nicely the expected state to which we have indirect access via THz absorption from the first excited state. Figure 5(c) shows the magnetic field effect between 92 and 98 cm^{-1}. Although the transmission spectra get more noisy, because we are reaching the limits of the detector, a magnetic effect is visible. We thus identify another peak P3 around 94 cm^{-1}, in excellent agreement with our calculations and optical spectra (see below). All the other resonances in the transmission spectrum [Fig. 5(a)] can be ascribed to phonon transitions, and no magnetic field effects were observed for them.

C. Magnetic circular dichroism and absorption spectroscopy

The determination of the four crystal-field parameters is still not possible without the complete splitting of the full ground multiplet, because infinite sets of parameter values can reproduce the data. The necessary level of additional information can be obtained using a combination of magnetic

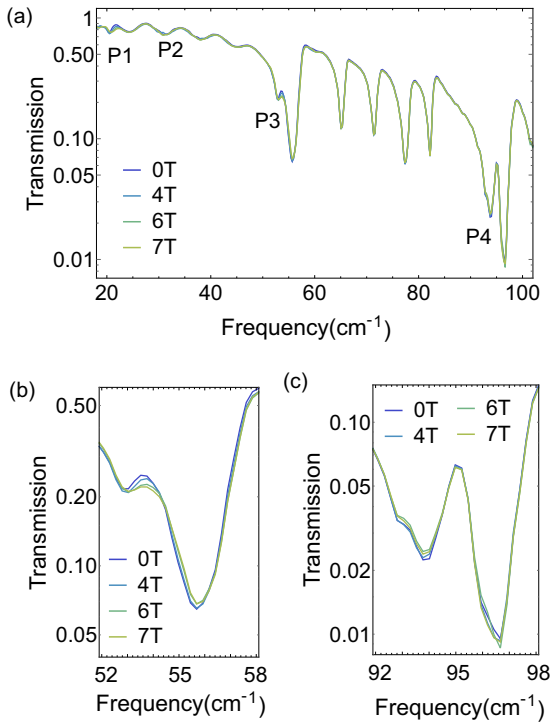

FIG. 5. Far-infrared spectra acquired on a pressed pellet sample (5 mm diamater) at 5 K, using 10.7 mg of the complex diluted in 41.2 mg of eicosane and prepared as a pressed pellet. (a) Spectrum measured in the whole 20–100 cm^{-1} region. (b) and (c) show zoom ins of the filed dependence of peaks that show magnetic field effects on the spectrum, in the spectral region not reachable with backwave oscillators (peaks P2 and P3, respectively).

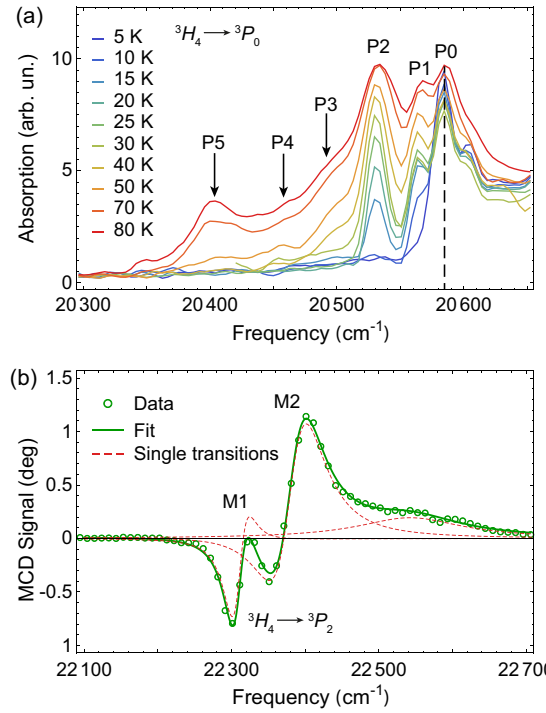

FIG. 6. (a) Absorption spectrum of $^3H_4 \rightarrow {}^3P_0$ between 5 and 80 K at zero field. (b) MCD spectrum of $^3H_4 \rightarrow {}^3P_2$ at 5 K. Two measurement sets at 10 and −10 T were subtracted from each other to account for spurious circular dichroism effects. The sample was prepared as micro-crystalline powder and fixed with paraffin on a quartz glass substrate.

circular dichroism (MCD) and variable-T absorption spectroscopy (VTA).

Many RE ions show rich absorption spectra in the visible region, caused by electric dipole transitions of $4f$ electrons [35,61], as described by Judd-Ofelt theory [62,63]. Thanks to the relatively narrow linewidth of f-f transitions, peak positions can be determined with good accuracy. For both types of measurements, we used an Aviv 42 CD spectrometer that is equipped with an Oxford Instruments Spectromag SM4000 with optical access and fields up to 10 T. A photomultiplier serves as detector in the visible range.

The splitting of the ground multiplet can be extracted from the T dependence of the excitation into the $^3P_0$ state, as shown in Fig. 6(a). At 5 K, only the ground state is populated, and only a single large peak at 20 585 cm^{-1} is thus visible. This peak is accompanied by satellite peaks at higher energies that arise from vibronic coupling. By increasing T, higher states within the ground multiplet $^3H_4$ become populated and give rise to additional peaks P1–P5. The energy differences between each of these excitation energies and the ground state transition afford the crystal-field splitting of the ground multiplet, given in Table I. The energies of P1 and P3 agree well, within experimental errors, with the results obtained by THz and far-infrared spectroscopy. As the resolution is lower in the visible regime, error bars are larger for those measurements.

As customary for REs [57], selection rules are relatively lax here and transitions to $^3P_0$ from all the different ground multiplet levels were observed, so that we cannot obtain any information about the nature of the involved states. To narrow down the number of possible solutions for the assignment of states, we performed MCD spectroscopy on the $^3H_4 \rightarrow {}^3P_2$ transition. As this excited multiplet has a total angular momentum of $J = 2$, it splits into three non-Kramers states, two of which are degenerate in zero-field. Since their splitting is determined by only one crystal-field parameter, B_0^2, the three remaining parameters can be fitted to the other spectroscopic results. Figure 6(b) shows the MCD spectrum at 10 and 5 K for the transition. A pure first-derivative Lorentzian line shape arises from a degenerate excited state in zero field, in literature also known as A term [64,65]. However, when the ground

TABLE I. Assignment of the optical peaks and summary of the spectroscopically determined zero-field splitting (ZFS) of the ground multiplet.

Peak	E (cm^{-1})	ZFS-VTA (cm^{-1})	ZFS-THz/FIR (cm^{-1})
P0	20 585 ± 1	0	0
P1	20 574 ± 1	21 ± 2	20.5 ± 0.1
P2	20 531 ± 1	54 ± 2	53.7 ± 0.2
P3	20 492 ± 2	93 ± 3	93 ± 1
P4	20 458 ± 5	127 ± 6	N.A.
P5	20 403 ± 1	182 ± 2	N.A.

state is a degenerate state in zero field, the line shape is best described by a combination of a Lorentzian and its first derivative. An applied magnetic field removes the degeneracy of the ground state, which results in an unequal population of the two states and thus to both different absorption strengths and resonance frequencies. This contribution is also known as C term in literature [64,65]. Higher-order effects, known as B terms, that result from field-induced mixing of states, are usually very small, and will be neglected in this analysis. Fitting of the data provides transition energies of 22 310.6 and 22 380.2 cm^{-1}, in the following referred to as M1 and M2, respectively. The Lorentzian line shape centered at 22 542.3 cm^{-1} accounts for all phonon-assisted transitions and will not be considered further. As shown in the analysis section, this distorted line shape, together with angle-resolved magnetometry, unequivocally identifies the ground state as a doublet and leads to the conclusion that the doublet ground state must be a superposition of $M_J = \pm 4$ and $M_J = \mp 2$.

III. ANALYSIS

A. The spin Hamiltonian

The total Hamiltonian for the Pr(III) $4f$ electrons can be expressed as a free-ion, unperturbed part H_{ion}, which describes the energy level structure without environmental effects, plus the crystal-field contribution H_{CF}:

$$H = H_{\text{ion}} + H_{\text{CF}}, \tag{2}$$

where H_{ion} is defined as

$$\begin{aligned} H_{\text{ion}} = E_{\text{AVE}} &+ \sum_{k=2,4,6} F^k f_k + \xi_{4\text{f}} A_{\text{SO}} + \alpha L(L+1) \\ &+ \beta G(G_2) + \gamma G(G_7) + \sum_{i=2,3,4,5,6,7,8} t_i T^k \\ &+ \sum_{k=0,2,4} m_k M^k + \sum_{k=2,4,6} p_k P^k, \end{aligned} \tag{3}$$

in which E_{AVE} describes any contributions of spherical symmetry, $F^k f_k$ describe electrostatic interactions, where F^k are the radial electrostatic repulsion integrals and f_k represent their angular part, and $\xi_{4\text{f}} A_{\text{SO}}$ describes the spin-orbit (SO) contribution. Two-particle interactions are accounted by α, β, and γ, $t_i T^k$ describe three-particle interactions, and $m_k M^k$ and $p_k P^k$ describe magnetically and electrostatically correlated spin-spin and spin-orbit interactions. The derivation, formalism, and analytical expressions for each of the terms are known from the literature [35].

The crystal-field Hamiltonian H_{CF} can be expressed, rather elegantly, as a sum of operator equivalents [36] that represent total orbital momentum operators. The derivation and significance of terms are currently the subject of revision [66]. However, J mixing, originally neglected in the operator equivalents method, might play a role in our system [35]. Due to J mixing, the wave functions of an $^{2S+1}L_J$ manifold have small contributions from those of other J, which affect the energy levels of our system. In the following, we thus stick to the notation originally introduced by Wybourne [67], and solve the Hamiltonian numerically via a fit. For D_{3h} symmetry, the even part of the crystal-field Hamiltonian, which determines the energy level splitting, is

$$H_{\text{CF}} = B_0^2 C_0^2 + B_0^4 C_0^4 + B_0^6 C_0^6 + B_6^6 \left(C_6^6 + C_{-6}^6\right), \tag{4}$$

with B_q^k representing the crystal-field parameters and $C_q^k = \sqrt{4\pi/(2k+1)}\, Y_q^k$ the Racah tensor operators, described in terms of spherical harmonics Y_q^k. For studying uncoupled Pr(III) ions, it is enough to consider crystal-field interactions until the order of $k = 6$, as higher orders vanish [35].

Finally, the crystal-field splitting of the ground multiplet can be determined by knowing the crystal-field parameters. In the following, multiplets will be named using the Russell-Saunders terms $^{2S+1}L_J$, where S represents the spin multiplicity, L the orbital momentum and J the total angular momentum, and corresponding states as $|M_J\rangle$, with M_J the magnetic quantum number. Due to the D_{3h} symmetry, the ground multiplet of Pr(III), $^3H_4$, is split into three degenerate doublet states and three nondegenerate singlet states, where states with $|\Delta M_J| = 6$ are mixed.

The states involved in the visible absorption can be obtained from selection rules for induced electric dipole transitions within the Judd-Ofelt theory framework. In this model, the excited state are not considered to be purely $4f^2$ states, but have admixtures of $4f^1 n'd$ and $4f^1 n'$g orbitals. The odd part of the crystal-field parameters plays a crucial role in the determination of selection rules. For D_{3h} symmetry, it is defined as [35]

$$\begin{aligned} H_{\text{CF}}^{(\text{odd})} = &\, \text{i}B_3'^3 \left(C_{-3}^3 + C_3^3\right) + \text{i}B_3'^5 \left(C_{-3}^5 + C_3^5\right) \\ &+ \text{i}B_3'^7 \left(C_{-3}^7 + C_3^7\right). \end{aligned} \tag{5}$$

The selection rules can be obtained from the evaluation of two 3j-Wigner elements, which are part of the transition matrix elements, defined as [61]

$$\begin{pmatrix} 1 & \lambda & k \\ \rho & -(\rho+q) & q \end{pmatrix}, \quad \begin{pmatrix} J & \lambda & J' \\ -M & -(\rho+q) & M' \end{pmatrix}. \tag{6}$$

The parameters q and k correspond to the indices of odd crystal-field parameters, B_q^k, in Eq. (5), λ is an even parameter, J, M and J', M' denote the ground and excited state quantum numbers, respectively, and ρ defines the polarization [0 for linearly, -1 for left-handed (lcp) and $+1$ for right-handed circularly polarized light (rcp)]. In general, $\Delta l = \pm 1$, $\Delta S = 0$, $\Delta L = 3 \leqslant 6$ and $\Delta J = 2 \leqslant 6$ are obeyed for the transition $^3H_4 \rightarrow {}^3P_2$. Finally, we obtain the selection rule

$$\Delta M = M' - M = -3 - \rho, \tag{7}$$

giving $\Delta M = -2$ for lcp light and $\Delta M = -4$ for rcp light. Peak M1 shows a stronger absorption of lcp light, while M2 shows a stronger absorption of rcp light. Peaks M1 and M2 shall thus correspond to $M_J = 0$ and $M_J = \pm 2$. Even with these considerations, we can see how over-parametrization affects the precise determination of the wavefunction: MCD data do not allow distinguishing between two possibilities: a dominant ground-state contribution of $M_J = 2$ leads to M1 with $M_J = 0$ and M2 with $M_J = \pm 2$, and is described by a positive value of B_0^2; the opposite is true for a dominant ground-state contribution of $M_J = 4$. We show in the following section how these uncertainties can be eliminated via a quantitative analysis of the crystal-field parameters that considers all the results of the multitechnique approach.

TABLE II. Calculated energies and wave functions of the states of the $^3H_4$ and $^3P_2$ multiplets using the crystal-field parameters obtained via the multitechnique iterative method (ite subscript). Comparison to the result of commonly used best fitting procedures of the susceptibility is provided (mag subscript). See Supplemental Material for higher excited states [68].

Peak	E_{exp} (cm^{-1})	E_{ite} (cm^{-1})	$\|\Psi_s\rangle_{ite}$	E_{mag} (cm^{-1})	$\|\Psi_s\rangle_{mag}$
P0	0	0	$0.85\|\pm2\rangle + 0.53\|\mp4\rangle$	0	$0.78\|\pm2\rangle + 0.63\|\mp4\rangle$
P1	20.5 ± 0.1	20.7	$0.71\|+3\rangle + 0.71\|-3\rangle$	22	$0.71\|3\rangle + 0.71\|-3\rangle$
P2	53.7 ± 0.2	54.5	$0.53\|\pm2\rangle - 0.85\|\mp4\rangle$	98	$0.78\|\pm4\rangle - 0.63\|\mp2\rangle$
P3	93 ± 1	92.4	$0.71\|+3\rangle - 0.71\|-3\rangle$	137	$\|\pm1\rangle$
P4	127 ± 6	112.9	$\|\pm1\rangle$	164	$0.71\|3\rangle - 0.71\|-3\rangle$
P5	182 ± 3	182.6	$\|0\rangle$	213	$\|0\rangle$
M1	$22\,311 \pm 1$	22 307.8	$\|0\rangle$		
–	–	22 336.4	$\|\pm1\rangle$		
M2	$22\,380 \pm 1$	22 381.1	$\|\pm2\rangle$		

B. Quantitative crystal-field analysis

The quantitative analysis of the crystal-field terms was carried out in several iterative steps. Using the computer program *f* shell [69], which is able to perform a fit of free-ion and crystal-field parameters to a given set of energy levels, we first determined the parameter B_0^2 from the data on the $^3P_2$ multiplet. This allows narrowing down the number of possible solutions for the three remaining parameters B_q^k. In the next step, we performed a fit of the T-dependent magnetization data using the widely used least-square fitting program CONDON [70]. It is well known that fitting of magnetic data suffers from overparametrization. It is thus useful to use the magnetic data not only as a part of a multitechnique investigation, but also to evidence what level of information can be extracted when in absence of spectroscopic data.

The magnetization data was fitted using CONDON [70] by considering perturbations with the first 91 states. We found that the low-T data, $T \leqslant 5$ K, can only be explained with a major contribution of $|M_J\rangle = |\pm 2\rangle$ species to the ground state. Considering the discussed selection rules in the previous section, we conclude that B_0^2 has to be positive and can be precisely fitted to the splitting of the $^3P_2$ multiplet. Furthermore, magnetization data suggests a $|M_J\rangle = |3\rangle + |-3\rangle$ as the first excited state separated by about 20 cm^{-1}, which falls in line with our spectroscopic observations.

Using these results, we moved on to analyzing the spectroscopic data of the ground multiplet using the obtained crystal-field parameters B_q^k as starting parameters. The spectroscopic data were then fitted under the constraints discussed in the previous section. Using a best-fit approach with the *f*-shell program [69], it is possible to obtain the following best set of parameters: $B_0^2 = 172$ cm^{-1}, $B_0^4 = -309$ cm^{-1}, $B_0^6 = -532$ cm^{-1}, and $B_6^6 = -273$ cm^{-1}. Better agreement with experimental data was found when E_{AVE}, ξ_{4f}, and F^2 [Eq. (3)] were additionally varied. The best fit was obtained for $E_{AVE} = 9\,945$ cm^{-1}, $\xi_{4f} = 758$ cm^{-1}, and $F^2 = 68\,469$ cm^{-1}, from which the energy level splitting shown in Table II can be calculated. The remaining free-ion parameters were fixed to reported values taken from Ref. [35]. Good agreement is found between measured and calculated energy levels, with only P4 slightly off the experimental error. Furthermore, the calculated THz transition energies in a magnetic field [inset in Fig. 4(a)] are overestimated. However, no other set of B_q^k parameters was found to adequately describe all the spectroscopic observations.

It is now instructive to compare how this result agrees with the fitting of the susceptibility versus T curve, which is a main tool currently used for the determination of the energy level splittings of REs in the chemical literature [71,72]. Two different sets of parameters were used for the magnetization fitting: a simplified model, which only considers the 33 states of the lowest-lying three multiplets $^3H_4$, $^3H_5$, and $^3H_6$, and an extended one that takes all $4f^2$ configurations (91 states) into account (see also Supplemental Material [73]). The energy levels of P0, P1, and P3 were all very well reproduced with the fitting of the susceptibility versus T curve. However, in both cases, the calculation slightly overestimates the magnetic moment in the mid-T regime around 50 K whenever a state is included in the energy region between 30 and 90 cm^{-1}. The state at 53.5 cm^{-1}, directly observed via THz and far-infrared spectroscopy, would thus be invisible to a mere fitting of the magnetic properties. Even higher discrepancies exists for the data calculated from the susceptibility fitting and those and observed at energies higher than 100 cm^{-1}. This is due to the fact that these states only become reasonably populated at $T > 100$ K, where μ_{eff} is already close to its theoretical maximum of $g_J\sqrt{J(J+1)} \approx 3.6\ \mu_B$. As a consequence these levels have a comparably small influence on the magnetic behavior, and their position is thus very difficult to assess via the magnetic data fitting procedure. It is thus clear that only spectroscopic tools can provide a reliable assessment of these higher excited states.

IV. CONCLUSIONS

Our results showed how a multitechnique investigation can provide the details of the spin structure of the magnetic levels of a lanthanide ion, and highlight the limitations and level of confidence of approaches that rely purely on magnetometry. The usual drawback of experimental approaches, namely, the high level of overparametrization present even for highly symmetrical compounds, has been overcome by using a combination of visible, THz and VTA spectroscopies

at low temperatures, together with magnetometry techniques. In particular, our iterative approach, exploiting both f-shell and CONDON programs, allows identifying all the necessary crystal-field parameters and to discriminate between different combinations of the wave functions. For the purposes of theoretical and computational *ab initio* studies, the parameters and techniques presented here offer an excellent experimental test ground for the validation of new numerical methodologies.

From the study we could also assess the level of confidence of best-fit procedures of susceptibility curves, routinely employed in the chemical literature. These are well-known to suffer from overparametrization, but they seem to provide a fairly good assessment of the energy levels below 30 K, where the measurement technique is most sensitive. The assessment of higher energy levels is far less accurate, even though these are usually less important for the interesting low-T dynamic region. More surprising is the inability of such procedures to identify the presence of states already around 50 K, which might play an important role in the spin relaxation processes and in the supposed Raman and Orbach mechanisms. These observations thus better quantify some of the limitations of the use of fitting of susceptibility data for the estimation of level spacings in REs, and highlight the importance of spectroscopic support for the determination of magnetic processes in REs.

While our analysis focuses on the determination of the crystal-field parameters of Pr(III) ions in hexagonal environments, the methodology illustrated is applicable in general, and can now be used to validate theoretical models of rare-earths in molecular and bulk compounds. Perspectively, it will be useful to apply these techniques to molecular systems such as RE-based phtalocyanine complexes, for which several level assignments have been proposed, or for the interpretation of surface effects from spectroscopic data [74,75]. The analysis described here can now be used as a stepping stone for the understanding and design the magnetic anisotropy in magnetic clusters and molecular nanomagnets. In particular, as the sensitivity limits of the spectroscopic techniques employed can be pushed to the monolayer level, these results also provide a way of assessing the spin behavior of REs on surfaces. Comparison to hypothesized anisotropy values, and theoretical surface-induced effects on REs would then be possible.

ACKNOWLEDGMENTS

We thank Wolfgang Frey for face indexing of the crystals. This work was financed by the Royal Society (URF and Research Grant), the AvH Stiftung (Sofja Kovalevskaja Prize), EPSRC (QuEEN grant), the European Research Council (ERC-StG-338258-OptoQMol), the Studienstiftung des Deutschen Volkes and the Deutsche Forschungsgemeinschaft (DFG, INST 41/864-1, SL104/5-1).

[1] J. Lu, M. Guo, and J. Tang, Chem. An Asian J. **12**, 2772.
[2] J. D. Rinehart and J. R. Long, Chem. Sci. **2**, 2078 (2011).
[3] D. N. Woodruff, R. E. P. Winpenny, and R. A. Layfield, Chem. Rev. **113**, 5110 (2013).
[4] K. A. Gschneidner, L. Eyring, and G. H. Lander, *Handbook on the Physics and Chemistry of Rare Earths* (Elsevier, North-Holland, Amsterdam, 2001), Vol. 32.
[5] N. Ishikawa, M. Sugita, T. Ishikawa, S.-y. Koshihara, and Y. Kaizu, J. Am. Chem. Soc. **125**, 8694 (2003).
[6] R. Sessoli and A. K. Powell, Coord. Chem. Rev. **253**, 2328 (2009).
[7] L. Bogani, J. Appl. Phys. **109**, 07B115 (2011).
[8] Y.-S. Meng, S.-D. Jiang, B.-W. Wang, and S. Gao, Acc. Chem. Res. **49**, 2381 (2016).
[9] J. M. Clemente-Juan, E. Coronado, and A. Gaita-Ariño, Mononuclear lanthanide complexes: Use of the crystal field theory to design single-ion magnets and spin qubits, in *Lanthanides and Actinides in Molecular Magnetism* (Wiley-VCH, Weinheim, 2015) Chap. 2, pp. 27–60.
[10] J. M. Frost, K. L. M. Harriman, and M. Murugesu, Chem. Sci. **7**, 2470 (2016).
[11] L. Bogani and W. Wernsdorfer, Nat. Mater. **7**, 179 (2008).
[12] L. Bogani, Experiments on molecular magnets for molecular spintronics, in *Molecular Nanomagnets and Related Phenomena*, edited by S. Gao (Springer, Berlin, Heidelberg, 2015), pp. 331–381.
[13] A. Bedoya-Pinto, S. G. Miralles, S. Vélez, A. Atxabal, P. Gargiani, M. Valvidares, F. Casanova, E. Coronado, and L. E. Hueso, Adv. Funct. Mater. **28**, 1702099 (2018).
[14] E. Heintze, F. El Hallak, C. Clauß, A. Rettori, M. G. Pini, F. Totti, M. Dressel, and L. Bogani, Nat. Mater. **12**, 202 (2013).
[15] S. Thiele, F. Balestro, R. Ballou, S. Klyatskaya, M. Ruben, and W. Wernsdorfer, Science **344**, 1135 (2014).
[16] S. Müllegger, S. Tebi, A. K. Das, W. Schöfberger, F. Faschinger, and R. Koch, Phys. Rev. Lett. **113**, 133001 (2014).
[17] Y.-S. Ding, N. F. Chilton, R. E. P. Winpenny, and Y.-Z. Zheng, Angew. Chem. Int. Ed. **55**, 16071 (2016).
[18] F.-S. Guo, B. M. Day, Y.-C. Chen, M.-L. Tong, A. Mansikkamäki, and R. A. Layfield, Angew. Chem. Int. Ed. **56**, 11445 (2017).
[19] C. A. P. Goodwin, F. Ortu, D. Reta, N. F. Chilton, and D. P. Mills, Nature (London) **548**, 439 (2017).
[20] C. Cervetti, E. Heintze, and L. Bogani, Dalton Trans. **43**, 4220 (2014).
[21] A. Cornia and M. Mannini, Single-molecule magnets on surfaces, in *Molecular Nanomagnets and Related Phenomena*, edited by S. Gao (Springer, Berlin, Heidelberg, 2015), pp. 293–330.
[22] R. J. Holmberg and M. Murugesu, J. Mater. Chem. C **3**, 11986 (2015).
[23] D. Gatteschi, R. Sessoli, and J. Villain, *Molecular Nanomagnets* (Oxford University Press, Oxford, New York, 2006).
[24] R. Bircher, G. Chaboussant, C. Dobe, H. Güdel, S. Ochsenbein, A. Sieber, and O. Waldmann, Adv. Funct. Mater. **16**, 209 (2006).
[25] X. Feng, C. Mathonière, I.-R. Jeon, M. Rouzières, A. Ozarowski, M. L. Aubrey, M. I. Gonzalez, R. Clérac, and J. R. Long, J. Am. Chem. Soc. **135**, 15880 (2013).

[26] S. Ohkoshi, S. Takano, K. Imoto, M. Yoshikiyo, A. Namai, and H. Tokoro, Nat. Photon. **8**, 65 (2014).

[27] S. Ohkoshi, K. Imoto, Y. Tsunobuchi, S. Takano, and H. Tokoro, Nat. Chem. **3**, 564 (2011).

[28] T. Mallah, S. Thiébaut, M. Verdaguer, and P. Veillet, Science **262**, 1554 (1993).

[29] F. Luis, F. L. Mettes, J. Tejada, D. Gatteschi, and L. J. de Jongh, Phys. Rev. Lett. **85**, 4377 (2000).

[30] M. Shiddiq, D. Komijani, Y. Duan, A. Gaita-Ariño, E. Coronado, and S. Hill, Nature **531**, 348 (2016).

[31] C. Schlegel, J. van Slageren, M. Manoli, E. K. Brechin, and M. Dressel, Phys. Rev. Lett. **101**, 147203 (2008).

[32] K. Bader, D. Dengler, S. Lenz, B. Endeward, S.-D. Jiang, P. Neugebauer, and J. van Slageren, Nat. Commun. **5**, 5304 (2014).

[33] D. Kaminski, A. L. Webber, C. J. Wedge, J. Liu, G. A. Timco, I. J. Vitorica-Yrezabal, E. J. L. McInnes, R. E. P. Winpenny, and A. Ardavan, Phys. Rev. B **90**, 184419 (2014).

[34] J. M. Zadrozny, J. Niklas, O. G. Poluektov, and D. E. Freedman, ACS Cent. Sci. **1**, 488 (2015).

[35] C. Görller-Walrand and K. Binnemans, in *Handbook on the Physics and Chemistry of Rare Earths* (Elsevier, North-Holland, Amsterdam, 1996), Vol. 23, pp. 121–283.

[36] K. W. H. Stevens, Proc. Phys. Soc. London A **65**, 209 (1952).

[37] J. J. Baldoví, S. Cardona-Serra, J. M. Clemente-Juan, E. Coronado, A. Gaita-Ariño, and A. Palii, J. Comput. Chem. **34**, 1961 (2013).

[38] N. F. Chilton, R. P. Anderson, L. D. Turner, A. Soncini, and K. S. Murray, J. Comput. Chem. **34**, 1164 (2013).

[39] L. Ungur and L. F. Chibotaru, Chem. Eur. J. **23**, 3708 (2017).

[40] F. Ortu, J. Liu, M. Burton, J. M. Fowler, A. Formanuik, M.-E. Boulon, N. F. Chilton, and D. P. Mills, Inorg. Chem. **56**, 2496 (2017).

[41] T. Pugh, N. F. Chilton, and R. A. Layfield, Chem. Sci. **8**, 2073 (2017).

[42] J. J. Baldoví, Y. Duan, R. Morales, A. Gaita-Ariño, E. Ruiz, and E. Coronado, Chem. Eur. J. **22**, 13532 (2016).

[43] J. J. Baldoví, Y. Duan, C. Bustos, S. Cardona-Serra, P. Gouzerh, R. Villanneau, G. Gontard, J. M. Clemente-Juan, A. Gaita-Ariño, C. Giménez-Saiz, A. Proust, and E. Coronado, Dalton Trans. **45**, 16653 (2016).

[44] L. E. Rosaleny and A. Gaita-Ariño, Inorg. Chem. Front. **3**, 61 (2016).

[45] J. van Slageren, S. Vongtragool, B. Gorshunov, A. A. Mukhin, N. Karl, J. Krzystek, J. Telser, A. Müller, C. Sangregorio, D. Gatteschi, and M. Dressel, Phys. Chem. Chem. Phys. **5**, 3837 (2003).

[46] J. van Slageren, New directions in electron paramagnetic resonance spectroscopy on molecular nanomagnets, in *EPR Spectroscopy: Applications in Chemistry and Biology*, edited by M. Drescher and G. Jeschke (Springer, Berlin, Heidelberg, 2012), pp. 199–234.

[47] Y. Rechkemmer, J. E. Fischer, R. Marx, M. Dörfel, P. Neugebauer, S. Horvath, M. Gysler, T. Brock-Nannestad, W. Frey, M. F. Reid, and J. van Slageren, J. Am. Chem. Soc. **137**, 13114 (2015).

[48] E. J. McInnes, Spectroscopy of single-molecule magnets, in *Single-Molecule Magnets and Related Phenomena*, edited by R. Winpenny (Springer, Berlin, Heidelberg, 2006), pp. 69–102.

[49] M. L. Baker, S. J. Blundell, N. Domingo, and S. Hill, Spectroscopy methods for molecular nanomagnets, in *Molecular Nanomagnets and Related Phenomena*, edited by S. Gao (Springer, Berlin, Heidelberg, 2015), pp. 231–291.

[50] R. Basler, C. Boskovic, G. Chaboussant, H. U. Güdel, M. Murrie, S. T. Ochsenbein, and A. Sieber, Chem. Phys. Chem. **4**, 910 (2003).

[51] F. Hulliger, M. Landolt, and H. Vetsch, J. Solid State Chem. **18**, 307 (1976).

[52] D. F. Mullica and E. L. Sappenfield, J. Chem. Crystallogr. **21**, 529 (1991).

[53] See Supplemental Material at http://link.aps.org/supplemental/10.1103/PhysRevB.99.134410 for crystallographic data in Sec. I.

[54] See Supplemental Material at http://link.aps.org/supplemental/10.1103/PhysRevB.99.134410 for magnetic data in Sec. II.

[55] F. El Hallak, J. van Slageren, J. Gómez-Segura, D. Ruiz-Molina, and M. Dressel, Phys. Rev. B **75**, 104403 (2007).

[56] J. van Slageren, S. Vongtragool, B. Gorshunov, A. Mukhin, and M. Dressel, Phys. Rev. B **79**, 224406 (2009).

[57] S. Haas, E. Heintze, S. Zapf, B. Gorshunov, M. Dressel, and L. Bogani, Phys. Rev. B **89**, 174409 (2014).

[58] B. Gorshunov, A. Volkov, I. Spektor, A. Prokhorov, A. Mukhin, M. Dressel, S. Uchida, and A. Loidl, J. Infrared Millim. Terahertz Waves **26**, 1217 (2005).

[59] U. S. Pracht, E. Heintze, C. Clauss, D. Hafner, R. Bek, D. Werner, S. Gelhorn, M. Scheffler, M. Dressel, D. Sherman, B. Gorshunov, K. S. Il'in, D. Henrich, and M. Siegel, IEEE Trans. THz Sci. Technol. **3**, 269 (2013).

[60] See Supplemental Material at http://link.aps.org/supplemental/10.1103/PhysRevB.99.134410 for further far infrared spectra in Sec. III.

[61] C. Görller-Walrand and K. Binnemans, in *Handbook on the Physics and Chemistry of Rare Earths* (Elsevier, North-Holland, Amsterdam, 1998), Vol. 25, pp. 101–264.

[62] B. R. Judd, Phys. Rev. **127**, 750 (1962).

[63] G. S. Ofelt, J. Chem. Phys. **37**, 511 (1962).

[64] C. Görller-Walrand and L. Fluyt, in *Handbook on the Physics and Chemistry of Rare Earths* (Elsevier, North-Holland, Amsterdam, 2010), Vol. 40, pp. 1–107.

[65] W. R. Mason, *A Practical Guide to Magnetic Circular Dichroism Spectroscopy* (Wiley, Hoboken, New Jersey, 2006).

[66] C. Rudowicz and C. Y. Chung, J. Phys.: Condens. Matter **16**, 5825 (2004).

[67] B. Wybourne, *Spectroscopic Properties of Rare Earths* (Interscience, New York, 1965).

[68] See Supplemental Material at http://link.aps.org/supplemental/10.1103/PhysRevB.99.134410 for a full calculation of the energy levels in Sec. IV.

[69] M. F. Reid, *F-Shell Empirical Programs* (University of Canterbury, Christchurch, New Zealand).

[70] H. Schilder and H. Lueken, J. Magn. Magn. Mater. **281**, 17 (2004).

[71] C. Ritchie, E. G. Moore, M. Speldrich, P. Kögerler, and C. Boskovic, Angew. Chem., Int. Ed. Engl. **49**, 7702 (2010).

[72] V. Chandrasekhar, P. Bag, M. Speldrich, J. van Leusen, and P. Kögerler, Inorg. Chem. **52**, 5035 (2013).

[73] See Supplemental Material at http://link.aps.org/supplemental/10.1103/PhysRevB.99.134410 for a calculation of the energy levels based on the CONDON parameters in Sec. V.

[74] N. Magnani, R. Caciuffo, E. Colineau, F. Wastin, A. Baraldi, E. Buffagni, R. Capelletti, S. Carretta, M. Mazzera, D. T. Adroja, M. Watanabe, and A. Nakamura, Phys. Rev. B **79**, 104407 (2009).

[75] R. Marx, F. Moro, M. Dörfel, L. Ungur, M. Waters, S. D. Jiang, M. Orlita, J. Taylor, W. Frey, L. F. Chibotaru, and J. van Slageren, Chem. Sci. **5**, 3287 (2014).